Our Magphan RT family continues to grow to meet QA needs for MR imaging of large fields of view.

The modular design enables the Magphan® RT phantom to be handled by a single person without special equipment. The three-piece configuration measures geometric distortion and uniformity along with tests for laser alignment, slice thickness, resolution, and Signal-to-Noise Ratio. The central section contains 24 contrast spheres that cover a range of T1, T2, and ADC values, as well as two slice thickness ramps.

The Phantom Laboratory manufactures high-precision phantoms coupled with Smári image analysis service and innovative custom solutions for the medical imaging and radiation therapy fields.

Click to view our phantoms and schedule a demo of our Smári image analysis service.

phantomlab

phantomlab.com

Received: 10 January 2021 | Revised: 22 September 2021 | Accepted: 10 October 2021

DOI: 10.1002/mp.15306

RESEARCH ARTICLE

MEDICAL PHYSICS

A comprehensive Monte Carlo study of CT dose metrics proposed by the AAPM Reports 111 and 200

Paulo R. Costa[1] | **Denise Y. Nersissian**[1] | **Nancy K. Umisedo**[1] | **Alejandro H. L. Gonzales**[1] | **José M. Fernández-Varea**[2]

[1] Institute of Physics, University of São Paulo, São Paulo, SP, Brazil

[2] Facultat de Física (FQA and ICC), Universitat de Barcelona, Barcelona, Catalonia, Spain

Correspondence
Paulo R. Costa, Institute of Physics, University of São Paulo, São Paulo, SP, 05508-090, Brazil
Email: pcosta@if.usp.br

Funding information
The São Paulo Research Foundation, Grant/Award Numbers: 2010/12237-7, 2018/05982-0; National Commission of Nuclear Energy, Grant/Award Number: 1341001551/2015; CNPQ, Grant/Award Numbers: 315096/2018-7, CNPQ/FAPESP; INCT - Metrology of Ionizing Radiation in Medicine, Grant/Award Number: 2008/57863-2; Spanish Ministerio de Ciencia, Innovación y Universidades, Grant/Award Number: PGC2018-096788-B-I00

Abstract

Purpose: A Monte Carlo (MC) modeling of single axial and helical CT scan modes has been developed to compute single and accumulated dose distributions. The radiation emission characteristics of an MDCT scanner has been modeled and used to evaluate the dose deposition in infinitely long head and body PMMA phantoms. The simulated accumulated dose distributions determined the approach to equilibrium function, $H(L)$. From these $H(L)$ curves, dose-related information was calculated for different head and body clinical protocols.

Methods: The PENELOPE/penEasy package has been used to model the single axial and helical procedures and the radiation transport of photons and electrons in the phantoms. The bowtie filters, heel effect, focal-spot angle, and fan-beam geometry were incorporated. Head and body protocols with different pitch values were modeled for x-ray spectra corresponding to 80, 100, 120, and 140 kV. The analytical formulation for the single dose distributions and experimental measurements of single and accumulated dose distributions were employed to validate the MC results. The experimental dose distributions were measured with OSLDs and a thimble ion chamber inserted into PMMA phantoms. Also, the experimental values of the $CTDI_{100}$ along the center and peripheral axes of the CTDI phantom served to calibrate the simulated single and accumulated dose distributions.

Results: The match of the simulated dose distributions with the reference data supports the correct modeling of the heel effect and the radiation transport in the phantom material reflected in the tails of the dose distributions. The validation of the x-ray source model was done comparing the $CTDI$ ratios between simulated, measured and CTDosimetry data. The average difference of these ratios for head and body protocols between the simulated and measured data was in the range of 13–17% and between simulated and CTDosimetry data varied 10–13%. The distributions of simulated doses and those measured with the thimble ion chamber are compatible within 3%.

In this study, it was demonstrated that the efficiencies of the $CTDI_{100}$ measurements in head phantoms with $nT = 20$ mm and 120 kV are 80.6% and 87.8% at central and peripheral axes, respectively. In the body phantoms with $nT = 40$ mm and 120 kV, the efficiencies are 56.5% and 86.2% at central and peripheral axes, respectively. In general terms, the clinical parameters such as pitch, beam intensity, and voltage affect the D_{eq} values with the increase of the pitch decreasing the D_{eq} and the beam intensity and the voltage increasing its value. The $H(L)$ function does not change with the pitch values, but depends on the phantom axis (central or peripheral).

Conclusions: The computation of the pitch-equilibrium dose product, $\hat{D}_{eq}$, evidenced the limitations of the $CTDI_{100}$ method to determine the dose delivered

by a CT scanner. Therefore, quantities derived from the $CTDI_{100}$ propagate this limitation. The developed MC model shows excellent compatibility with both measurements and literature quantities defined by AAPM Reports 111 and 200. These results demonstrate the robustness and versatility of the proposed modeling method.

KEYWORDS
computed tomography, CT dosimetry, Monte Carlo modeling

1 | INTRODUCTION

In the last two decades, x-ray computed tomography (CT) has become one of the most important diagnostic imaging methods. The capabilities of the CT technique increased its popularity around the world. Data from the Organization for Economic Co-operation and Development (OECD) demonstrates a growth of 12% in the number of CT procedures per inhabitant in the last five years.[1] This increase of CT procedures represents a considerable advance on improving the diagnostic of diseases, but turned on the alert to the possible negative consequences of larger populations being exposed to x-ray radiation from this imaging modality. According to the NCRP Report 184,[2] CT procedures represents 9.5% of all diagnostic medical examinations performed in adults in the United States. As CT procedures are not yet a low-dose modality,[3] the development of global dose evaluations and procedure optimizations are important tasks.[4,5]

As the direct measurement of the patient absorbed dose is complex, alternative methods have been proposed to indirectly estimate the patient dose. In this context, a consistent historical review on CT dosimetry was recently presented by Dixon.[6] For instance, a restricted definition of the computed tomography dose index (CTDI), the $CTDI_{100}$ index, was proposed as a practical indicator of patient dose and subsequently generalized as a "weighted average," $CTDI_w$, to be consistent with the differences of the measured values in the center and periphery of the phantoms.[6,7] The advent of multiple-row detector CT (MDCT) made necessary the introduction of an additional CT dose quantity, the volumetric-CTDI, $CTDI_{vol}$.[8] Its definition, $CTDI_{vol} = p^{-1}\ CTDI_w$ is also based on $CTDI_{100}$ and includes the effect of *pitch*, $p = b/nT$, where b is the table displacement per gantry rotation (for the helical scan mode) or the midpoint-to-midpoint spacing between successive scans (for the axial scan mode) and nT is the active detector length. $CTDI_{vol}$ estimates the average absorbed dose within the middle portion of the irradiated volume of a CT acquisition and represents the average dose over the central scan plane (at $z = 0$) for a 100 mm scan length.[8–10] Therefore, for a better representation of the overall energy (or dose) deposition, another descriptor, the dose length product, $DLP = L \times CTDI_{vol}$, was introduced. The DLP does not depend on b because the scanning length is given by $L = nb$ (n is the number of gantry rotations) and $CTDI_{vol}$ is proportional to b^{-1}.

All CTDI-based measurement methods use cylindrical polymethyl methacrylate (PMMA, $C_5O_2H_8$, $\rho = 1.19$ g/cm^3) phantoms of 16 cm or 32 cm diameter when head or body CT examinations are considered, respectively.[11,12] Due to the variety of patient sizes, $CTDI_{vol}$ is not a good descriptor of the actual absorbed dose to the patient. This fact has an important repercussion, especially in pediatric patients, in which the computation of absorbed dose based on the $CTDI_{vol}$ displayed by the CT device could underestimate the patient dose by a factor of 2–3 if a 32-cm PMMA phantom is used as reference.[13,14] In order to take this anatomical variability into account, the Size Specific Dose Estimate (*SSDE)* was introduced in the AAPM Report 204,[15] updated in the AAPM Report 220,[16] and ratified in the AAPM Reports 246[17] and 293.[18] It takes into account the patient size in the assessment of a quantity proportional to the patient absorbed dose from a CT examination.

Boone[19] defined the *efficiency*, ε, as the capability of the $CTDI_{100}$ metrics to assess the dose determined using the 100 mm chamber, compared to an infinitely long ion chamber. He also identified that the efficiencies are reduced for beam widths above 40 mm and decrease dramatically for beam widths above 100 mm. Even for beam widths less than 40 mm, the efficiency is reduced. Boone[19] reported that, for the center and peripheral positions of a 32-cm diameter PMMA phantom, the $CTDI_{100}$ can underestimate the dose by 63% and 88% with respect to the CTDI estimated considering an infinitely long ion chamber. Actually, the rapid evolution of CT detector technology already allows the use of x-ray beams broader than the 100 mm length of the pencil ion chamber employed in the $CTDI_{100}$ measurement, rendering the $CTDI_{100}$ paradigm completely unsuitable for characterizing the dose for those beam widths.[8,9] Hence, dose metrics derived from the $CTDI_{100}$ cannot represent accurately the doses associated to contemporary CT examinations.[20]

A comprehensive theory predicting relative dose distributions in cylindrical dosimetry phantoms associated to axial and helical CT scan series was developed by Dixon et al.[21,22] This formalism allows to derive CT dose

descriptors applied to cylindrical phantoms that solve the limitations and expand the applicability of the traditional (and current) quantities based on the $CTDI_{100}$ methodology.[23,24] The AAPM Report 111[9] proposed a unified methodology for CT dose descriptions built on this analytical formulation of dose distribution in cylindrical phantoms.

CT dose theory suggests the adoption of a new measurement paradigm to assess the maximum dose at the central point of the scanning length using a thimble ion chamber. The maximum dose as a function of the scanning length gives an additional dose description of the CT acquisition and protocol. Previous studies reported the accuracy of the novel metrics when compared to the $CTDI_{100}$ methodology for patient table translation and no-translation techniques.[22,25]

The AAPM Report 200[10] clarified the limitation and caveats of the $CTDI_{100}$ methodology to correctly represent the dose characteristics of modern CT systems. This publication presents measurement methods that overcome the limitations of the traditional $CTDI_{100}$-based procedure and the design of a general-purpose phantom, which was previously defined by AAPM and ICRU.[26] These methods provide the basis for medical physicists to review their practical establishment of dose properties of CT devices in the near future.

In the present study, Monte Carlo (MC) calculations have been done to obtain the dose distribution in infinitely long cylindrical PMMA phantoms of 16 cm and 32 cm diameters ensuing from modeling of axial and helical CT acquisitions of an MDCT. The MC modeling for the radiation emission characteristics of the MDCT scanner estimates the attenuation profile considering head and body bowtie filters, heel effect, focal spot size, and x-ray spectrum. The simulations were implemented according to the recommendations of the AAPM Reports 195[27] and 268.[28] Besides, an experimental validation of the MC dose distributions was made by means of a thimble ion chamber and OSL dosimeters measurements. The supplemental material #1 presents a flowchart describing the main parts of the work.

The AAPM Report 111 dose descriptors were computed from the simulated accumulated dose distributions. Specifically, the equilibrium dose, D_{eq}, the equilibrium scanning length, L_{eq}, and the pitch-equilibrium dose product, $\hat{D}_{eq}$, were derived from the equilibrium function, $H(L)$. In the present investigation, the computation of these metrics used cylindrical 14.5 cm long and 32 or 16 cm diameter PMMA phantoms that are already employed in CT quality control, as a complementary method to the use of the 60 cm long and 30 cm diameter ICRU/AAPM polyethylene phantom proposed by the AAPM Report 200. These results allow the verification of the radiation outputs in clinical facilities by means of the conventional CTDI phantoms and the AAPM Report 200 methodologies.[29]

The first contribution of the present article is the multiple-validation strategy of the MC model using different approaches. The second contribution lies on the application of the AAPM Reports 111 and 200 methodologies using traditional PMMA phantoms and its potential association with the migration process from the traditional $CTDI_{100}$-based method to the new proposed quantities using the ICRU/AAPM phantom.[10] These contributions can improve the progress of the current investigations associating approach-to-equilibrium related information to organ doses and to accelerate the development of frameworks associating these new quantities with SSDE and image quality information, looking to CT protocol design optimization. The association of these dose assessment metrics and the recently published methods for performance evaluation[30,31] are practical tools to improve the balance between patient dose and image quality in CT.

2 | MATERIALS AND METHODS

2.1 | Monte Carlo modeling

MC benchmarks have been developed in the last decades to simulate various aspects of CT techniques.[32,33] In the present study, MC simulation has been used to compute single dose distributions, $f(z)$, and accumulated dose distributions, $D(z)$, that were applied to calculate the derived dose CT metrics defined in the AAPM Reports 111 and 200.[9,10] The MC code PENELOPE/penEasy versions 2014/2015[34,35] was chosen to simulate the coupled electron–photon transport in infinitely long cylindrical PMMA phantoms for photon energies ranging from 15 keV to 140 keV. In these MC simulations, Phase Space Files (PSFs) containing the physical information of all particles that went through the pre-patient collimator were generated. PSFs are extensively used in radiotherapy research,[36] for treatment planning and dosimetry purposes,[35,37–39] and to implement radiation source models in CT.[40–42] Details on the approach to estimate the latent variance of a PSF can be found in appendix 2 of Sempau *et al*.[43]

The implementation of the MC simulation was done in a three-step process: (i) modeling the irradiation configuration of the CT system; (ii) simulating the radiation transport in the cylindrical PMMA phantom; and (iii) calibration of the simulated distributions in air-kerma units.

Table 1 summarizes the main information regarding the simulation modeling in compliance with the guidelines for presentation of adopted conditions and parameters according to the AAPM Report 268.[28] The employed MC methods were tested and validated by reproducing case 4 of the AAPM Report 195. In this test, MC simulations were carried out for a 32-cm

TABLE 1 Summary of the main information regarding the MC simulations[27]

Item name	Description
Code, version/release date	PENELOPE (v. 2014)/penEasy (v. 2015-05-30)
Validation	Comparative results of the energy deposited in PMMA phantoms according to AAPM Report 195
Timing	5×10^4 s approximately for the helical protocol • Intel Xeon CPU E5-2420. 1.9 GHz (12 CPUs) • Intel Xeon CPU E3-1270. 3.5 GHz (8 CPUs)
Source description	Phase Space File: • Fan beam geometry from one-dimension focal spot of 0.9 mm • Photon emission along the *y*-axis, without modulation. Distributed inside the fan angle. • Anode self-attenuation/heel effect • X-ray spectrum generated by the semiempirical TBC model with 0.1 keV bin • Head and body bowtie filter incorporated
Cross-sections	PENELOPE default: XCOM and EPDL (or PHOTOABS)
Absorption cutoff energies	Photons: EABS = 0.2 keV Electrons: EABS = 10 keV
Cutoff parameters	Elastic collisions: $C_1 = C_2 = 0.1$ Inelastic interactions: $W_{CC} = 1$ keV Bremsstrahlung: $W_{CR} = 0.1$ keV
Scored quantities	Energy imparted, 3D dose distributions
# histories	PSF generated from 10^9 histories
Statistical uncertainty	1% in the dose distributions simulation
Postprocessing	MatLab R2012a (Mathworks, inc. Natick, MA, USA) developed routines

TABLE 2 Technical specifications of the GE Discovery CT750HD[44]

Focus-isocenter distance, *F* (mm)	541
Focus-collimator distance, F_c (mm)	162
X-ray tube	GE Performix
Focal spot size (mm^2), see the IEC 60336/2006 standard	0.9×0.9
Anode angle	7°

diameter body PMMA phantom considering a monoenergetic 56.4 keV photon source and a tungsten target 120 kV spectrum filtered by 6 mm aluminum. The PENELOPE/penEasy results corresponding to the four contiguous cylindrical detectors benchmark of case 4 test 1[27] agreed better than 1.9% for both monoenergetic and spectral source at 10 and 80 mm collimations. PENELOPE/penEasy results for case 4 test 2 agree better than 2.2% and 1.7% for the detector in the periphery and at the center, respectively, for all collimations and sources.

2.1.1 | Step 1: MC model for the CT x-ray emission system

The GE Discovery CT750HD (General Electric Company, Boston, USA) system was taken as reference to model the x-ray emission. Some technical and geometrical characteristics of this equipment are given in Table 2.[44]

Most of the x-ray source models in diagnostic dosimetry assume that the x-rays are emitted from a point source, disregarding the focal spot size, angle of the target surface, and heel effect.[45–47] These characteristics have been implemented in the present x-ray source model. Figure 1a shows the modeled components attempting to represent the GE Discovery CT750HD CT system. The geometry was coded according to the PENGEOM format and syntax.[34,48]

Focal spot

A one-dimensional focal spot (line focal spot) of 0.9 mm length and 7° anode angle in the *z*-direction was implemented. The one-dimensional focal spot was positioned 3.4 μm beneath the surface of a tungsten block so as to include the anode self-attenuation in the source model. This depth was deduced from the comparison of the simulated primary profile and the analytical one in order to reproduce the heel effect on the primary profile. The x-ray spectra were generated utilizing the semi-empirical TBC model,[49–51] and the selected total filtrations were validated by Compton spectrometry and half-value layer (HVL) measurements (see Section 2.2.1).

Bowtie filter

Different strategies have been published to evaluate the bowtie filter effect on the dose distributions.[47,52–54] Figure 1b illustrates the geometrical characteristics and dimensions of the modeled bowtie filter, which was constructed as a truncated rectangular pyramid of

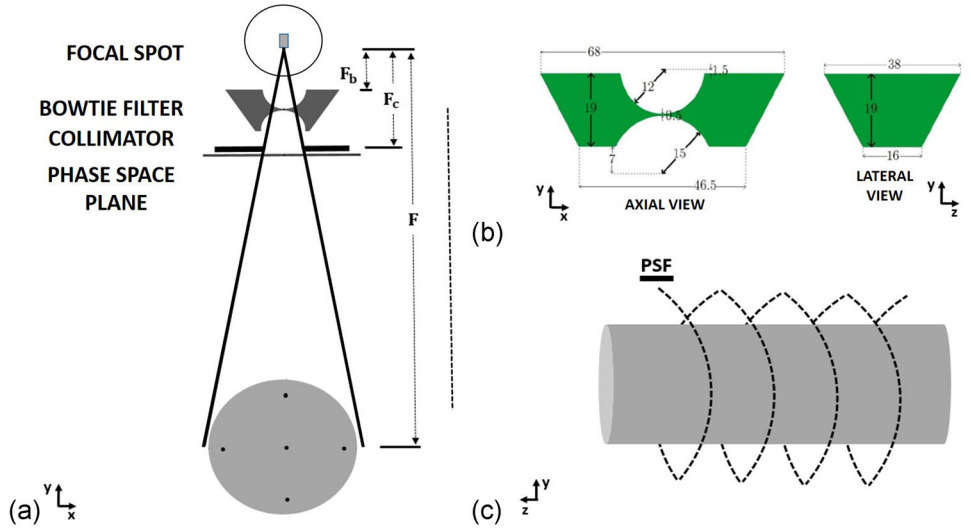

FIGURE 1 (a) Schematic representation of the modeled x-ray source components and the cylindrical phantom. The phase space plane is indicated. (b) Geometrical characteristics and dimensions from axial and lateral views of the modeled bowtie filter. All dimensions are in millimeters. (c) Representative path followed by the PSF around a cylindrical phantom implemented to model a helical CT scan acquisition

aluminum with two cylindrical sections removed. The adopted method uses only one designed bowtie filter that can represent real head and body bowtie filters by a careful choice of its relative position between the focal spot and the pre-patient collimator.[55] The optimal position can be established assessing the resulting homogenization properties reflected on the energy deposited in the simulated detector matrix for each head and body protocols.

The validation of the bowtie filter characteristics was done using MC modeled head and body CTDI phantoms. Two procedures were employed to evaluate the adequacy of homogenization of the absorbed dose in the CT detectors considering head and body protocols. First, each of the 15 PSFs generated combined to both head and body CTDI phantoms and, in each case, the energy deposited in each CT detector was scored. For each combination, the relative distance between the focal spot and the bowtie filter was increased from 1 to 15 cm in steps of 1 cm. For all simulations, the energy deposited in each detector element was tracked and compared. Finally, the two PSFs representing the best uniform energy deposition in all detector elements considering head and body protocols were selected.[56]

A second procedure was adopted to validate the bowtie filter positions. In this case, direct comparisons between simulated and measured $CTDI_{100}$ assessed in the central and peripheral positions of the head and body phantoms were performed. At this step, just the PSFs that produce the best homogenization in the arrangement of detectors were chosen for the evaluation. After each simulation, the ratios of center to peripheral absorbed doses were computed and compared with experimental results.

Collimator

Two 0.5 cm lead plates were designed with PENGEOM to model the collimator used in CT systems to produce a fan beam. No radiation transport in the collimator material was considered. The collimator was located at a distance F_c = 162 mm from the focal spot (Figure 1a and Table 2).

2.1.2 | Step 2: Simulation of CT central and peripheral dose distributions for single axial and helical CT scans

The second stage used the calculated PSFs to simulate the irradiation of the cylindrical phantoms and to compute the corresponding absorbed dose distributions. For this purpose, subroutines PSFSource and PSFSinisrc of the sourcePhaseSpaceFile.F module in the main program penEasy were modified to implement the rotation of the PSF around the axis of reference (AOR) and the translation along the *z*-axis (CT helical scan mode). All particles stored in the PSFs were evaluated.

For both, head and body phantoms, the 3D spatial dose distribution inside the phantoms were evaluated with the *tallySpatialDoseDistrib* in penEasy.[35] The single axial and helical dose distributions along the central and peripheral axes were extracted from the calculated 3D dose distribution by means of postprocessing routines developed in MatLab R2012a (Mathworks, inc. Natick, MA, USA). The voxel sizes were 1 cm (*x*-axis), 1 cm

(*y*-axis), 0.1 cm (*z*-axis). The methodology employed implies the determination of single axial dose distributions along the central and peripheral axes of head and body cylindrical PMMA phantoms. These central and peripheral dose distributions were computed from a 360° single rotation of the PSF in intervals of 1° around each phantom. To implement the helical scanning, the longitudinal position of the particle along the scanning length and the angular position around the axis of rotation was randomly sampled. Both, longitudinal and angular position were linked using the pitch value for each helical CT protocol. Instead of moving the phantom along the AOR as in a real CT scan, the *z*-coordinate of the particles was translated sampling uniformly the total scanning length.

TABLE 3 Clinical body and head protocols chosen to be modeled by MC simulation

Parameter	Protocols	
	Body	Head
Voltage (kV)	80, 100, 120, and 140	80, 100, 120, and 140
Rotation time (s)	1.0	1.0
Pitch	0.516, 0.984, and 1.375	0.531, 0.969, and 1.375
Bowtie filter	Body	Head
Collimation (mm)	40	20
Number of images per rotation	64	32
Detector array width (mm)	0.625	0.625

2.1.3 | Step 3: Calibration of the simulated dose distributions

The calibration of the central and peripheral dose distributions computed by MC simulation was done using the corresponding reading of a 10-cm pencil ion chamber. In this work, a simulated dose profile in terms of absorbed dose (eV/(g.hist)) was calibrated into air-kerma units by multiplication by a calibration factor. This factor is defined as the quotient between the integral of the 10 cm central interval of the simulated dose profile and the air-kerma length product determined by measurements.

2.2 | Validation of the MC results

The MC model was validated comparing its outputs in terms of central and peripheral dose distributions to analytical calculations and measurements. The conducted measurements were $CTDI_{100}$ and $CTDI_{100,air}$ using a 10-cm long ionization chamber and the determination of dose distributions with OSL ribbons and a thimble ionization chamber. The data were collected considering clinical settings (Table 3) and were compared with the MC simulation results. The measurements were carried out at the Institute of Radiology of the School of Medicine of the University of São Paulo (Brazil). A flowchart presenting these validation steps is included in the supplemental material #1.

2.2.1 | Validation using analytical equations

The analytical equations derived by Dixon and Boone[6,25] corresponding to the primary, scatter and total dose distributions, and recalled in the supplemental material #2 were implemented in MatLab environment. The primary profile allows to characterize the adequacy of some elements of the x-ray tube system and the geometric characteristics of the simulated CT system. This is possible as the primary profile shape is influenced by the heel effect, anode angle, of the focal spot size, and x-ray spectrum. Primary and total dose distributions along the central and peripheral axes of a CTDI phantom were computed using the x-ray source model.

Primary distributions, $f_p(z)$, normalized by the dose profile at $z = 0$, $f_p(0)$, were simulated. For the primary profile, the photon cut-off energy was set at 140 keV so as to absorb all photons delivered and to avoid secondary particles and improve the photon statistics.

Additionally, the x-ray spectra generated with the semi-empirical TBC model[49–51] were validated by comparison to those measured by Terini et al. employing a Compton spectrometer[57] and also to other x-ray spectra generator models.[58,59] Another cross-check was done comparing the HVLs resulting from the TBC model and measurements made with an ionization chamber in the GE Discovery CT750HD system at the same voltages.

To validate the adequacy of the simulation configuration, several simulated single dose distributions were compared to those from the analytical formulas. The scatter component originates from the deposited dose due to the detection of photons scattered by the phantom material. The preliminary validation of the x-ray source model was performed by comparison between analytical and simulated single dose distributions produced by beam widths of 10, 20, and 27 mm along the central axis of the cylindrical phantom.

2.2.2 | Validation using $CTDI_{100}$,$CTDI_{100,air}$, and CTDosimetry data

A second method to validate the MC simulations was done using both experimental CTDI measurements and CTDosimetry[60] published data. The experimental

method for determining the $CTDI_{100}$ is described in detail in the IAEA/TRS 457[23] and AAPM Report 96.[24] Besides, measurements of CTDI free-in-air ($CTDI_{100,air}$) yielded normalization factors for the $CTDI_{100,c}$ (c = central) and $CTDI_{100,p}$ (p = peripheral), and to assess the CT radiation emission at the isocenter without the scatter medium.

This validation procedure was done comparing the ratios of $CTDI_{100}$ in the central and periphery positions in head and body phantoms, $CTDI_{100,c}/CTDI_{100,p}$, and the ratios of weighted-$CTDI_{100}$ and $CTDI_{100}$ free-in-air, $CTDI_w/CTDI_{100,air}$, obtained from simulated and measured data using the GE Discovery CT750 HD scanner. The ratio $CTDI_{100,c}/CTDI_{100,p}$ evaluates the dose distribution inside the CTDI phantom and the ratio $CTDI_w/CTDI_{100,air}$ evaluates the CT radiation output.

For this part of the validation, the simulated dose profile computed in terms of eV/(g·hist) was calibrated using head and body PMMA phantoms measurements. A pencil ionization chamber (model 10 × 6-3CT, S/N 05–1151) with 10 cm of active length and 3 cm^3 of active volume was employed coupled to a digitizer module Accu-Gold+ (model AGDM+, S/N 48–1054) both manufactured by the Radcal, Co. (Radcal Inc, Monrovia, CA). The set was calibrated in a traceable Secondary Standard Dosimetry Laboratory.[61] The components of the type B uncertainty of this device were its calibration accuracy (±4%, at 150 kV and 10.2 mmAl HVL) and energy dependence (±5%, 3–20 mmAl HVL). Consequently, the propagated uncertainty of 6.4% for each ion chamber reading was considered.

2.2.3 | Validation from single and accumulated dose distributions with OSL dosimeters

Optically stimulated luminescence dosimeters (OSLD) have been employed to evaluate dose characteristics of CT systems.[62–64] In particular, dose profile measurements were done inserting OSL ribbon dosimeters into the central and peripheral holes of the CTDI phantoms. Luxel™ OSL dosimeters manufactured by Landauer (Landauer, Inc., Glenwood, USA) composed by Al_2O_3:C converted into powder and deposited over long plastic tapes with 0.3 mm in thickness[65] were used for this purpose. The tapes were fractionated into ribbons of approximately 20 cm length. These ribbons were covered by a black plastic to protect the dosimeters from environmental light. Technical details of the reader system are presented in supplemental material #3.

Around 80 ribbons were employed to validate the MC simulations. The signal registered by the OSL reader along the length of the ribbons is proportional to the x-ray fluence that reaches the corresponding ribbons at the central and peripheral axes of the CTDI phantom. In addition, this kind of OSL dosimeter (Al_2O_3:C) has a linear response with the radiation exposure that was subdued. The linearity and energy response of the OSL dosimeters had been investigated previously by Giansante et al.[66] The uncertainties associated to the OSL reading process were evaluated resulting in values lower than 5%.

Figure 2 depicts the experimental setup mounted to measure the primary dose distributions. The free-in-air measurement of a primary dose profile was carried out without CTDI phantom. The OSL ribbons into a PMMA rod of 1.0 cm diameter was aligned along the CT AOR and supported by a CTDI phantom (see Figure 2a and b). The patient positioning lasers were utilized to align the OSL ribbons. Primary distributions using head bowtie filter were measured adopting a nominal beam width of nT = 20 mm. The tube current and irradiation time for the primary profile measurements were 200 mA and 10 s, respectively.

Figure 2c shows the experimental setup used to measure the accumulated dose distributions for helical protocols employing both OSL ribbons and a thimble ion chamber (described in the next section). Three head or body phantoms were tied using long PMMA rods inserted through the holes used to positioning ion chambers or OSL ribbons. The alignment was done by centering the phantom in the middle of the gantry with the aid of the CT laser beams. Five PMMA rods containing an OSL ribbon each were introduced in the five holes of the CTDI body phantom. The tube current and irradiation time for the measurements of each set of dose distributions were 200 mA and 20 s, respectively. The procedures for measuring dose distributions in the head phantom were the same as those used in the body phantom.

2.2.4 | Validation based on thimble ion chamber measurements

For this purpose, a 10 × 6-0.6CT ion chamber (S/N 02–4831) coupled to a digitizer module Accu-Gold+ (model AGDM+, S/N 48–1054) both manufactured by the Radcal, Co. was used. As proposed by AAPM Reports 111[9] and 200,[10] the thimble ion chamber was carefully centered into the three-section body phantom and scans were made using the procedures defined in Table 3 . In particular, the step-by-step procedure defined in AAPM Report 200 was followed. A body protocol (Abdomen – up to 110 kg) was selected with 120 kV, 300 mA, 64 × 0.625 mm as collimation, pitches of 0.516 and 0.984. The dose rate profile was measured with the chamber located in the center and in the periphery of the three-section body phantom for scan lengths of 100, 150, 240, 350, and 450 mm. The detector response curves, which are proportional to the accumulated dose distributions, were compared to the simulated ones.

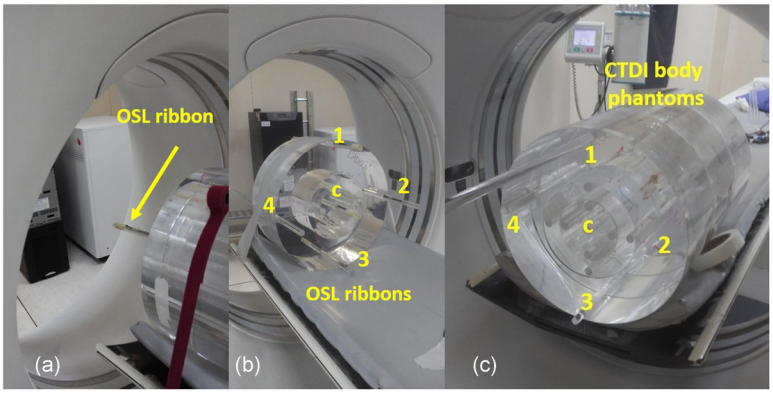

FIGURE 2 (a) and (b) Experimental setup used to measure the free-in-air primary dose distributions. The numbers 1–4 represent the peripheral holes and the letter c the central hole of the phantoms. The arrangement was adopted for measurements of the head primary dose profile carried out without CTDI phantom attenuation and scatter. The OSL ribbons were fixed into a PMMA rod of 1.0 cm diameter that was aligned along the CT AOR and supported by a CTDI phantom, and (c) experimental setup used to measure the accumulated dose distributions for helical protocols using the OSL ribbons and a thimble ion chamber. In this case, three head or body phantoms were tied using long PMMA rods inserted through the holes used to positioning the CTDI ion chambers

2.3 | Assessment of AAPM Reports 111 and 200 dose metrics from the accumulated dose distributions

The main dose metrics defined in AAPM Reports 111 and 200 are summarized in the supplemental material #2. The analytical expression of the approach-to-equilibrium function, $H(L) = D_L(0)/D_{eq} = 1 - \alpha e^{\frac{-4L}{L_{eq}}}$, suggest fittings using a parametric model. Specifically, the parametric model proposed in AAPM Reports 111 and 200 was used to fit these approach-to-equilibrium functions. The adjustable parameters α and L_{eq} were delivered by the Nonlinear Curve Fitting tool of the Origin 2020 software (OriginLab Corporation, Northampton, MA, USA). According to Boone,[46] α is the scatter fraction at the D_{eq}, which is related to the scatter to primary ratio, η, at the D_{eq} by $\alpha = \eta/(1+\eta)$. By convention, L_{eq} is the scan length where $H(L) = 0.98$. This method was compared to the procedure proposed in Appendix 5 of the AAPM Report 200[67] providing consistent results into 5% on the fitting parameters. In an infinitely long cylinder, both D_{eq} and L_{eq} depend on the radial distance to the central axis. The fitting routine was applied to each set of points corresponding to specific pitch values, tube voltages, CTDI phantoms, and for center, peripheral, and weighted $H(L)$. Using these $H(L)$ curves, the following dose-related information were accessed for the studied clinical protocols: L_{eq}, D_{eq}, and α. The equilibrium dose-pitch product $\hat{D}_{eq}$, defined in the supplemental material #2, was also evaluated.

3 | RESULTS

3.1 | Validation of the CT model and calibration of the simulated distributions

3.1.1 | Validation of the focal spot model

As presented in Section 2.2.1, the validation of the focal spot model was based on comparisons between simulated primary distributions and the corresponding analytical ones. The average differences between analytical and simulated primary distributions across the z-axis were estimated to be less than 1% for all studied beam widths.

The x-ray spectra used in the present work[49–51] were validated by comparison with those measured by Terini et al. employing a Compton spectrometer,[57] to TASMICS[58] and SpekPy[59] x-ray spectra generator models and by comparing the corresponding measured HVL values. The average differences between the experimental and semi-empirical spectra were less than 16% in the energy range from 20 to 140 keV. The comparison between the TBC and the other x-ray spectra generators resulted in average differences lower than 6% for the energies of interest. Finally, the average difference in measured and calculated HVLs were 5% for the body bowtie filter and 9% for the head bowtie filter.

3.1.2 | Validation based on the analytical dose distributions

Figure 3a compares analytical and simulated dose distributions that were produced from beam widths of 10, 20, and 27 mm on the central axis of a 32-cm cylindrical phantom. Figure 3b illustrates the contribution of the primary and scatter components on the dose distribution and shows a comparison with simulated profile for 27 mm beam width. The simulation was done for a 120 kV x-ray spectrum.

Defining a as the collimator aperture projected onto the z axis, magnified by the factor $M = F/F_c$, where F and F_c are the distances from source to the isocenter and to the collimator, respectively, and considering a small rectangular focal spot of uniform intensity, this parameter represents the width along the AOR of the pre-patient z-axis collimator geometrically projected from the centroid of the x-ray source. In this case, the parameter a is the full width of the beam at half its value at $z = 0$.[21,22] The collimator apertures, w, were computed from $a = Mw$. For instance, in the GE

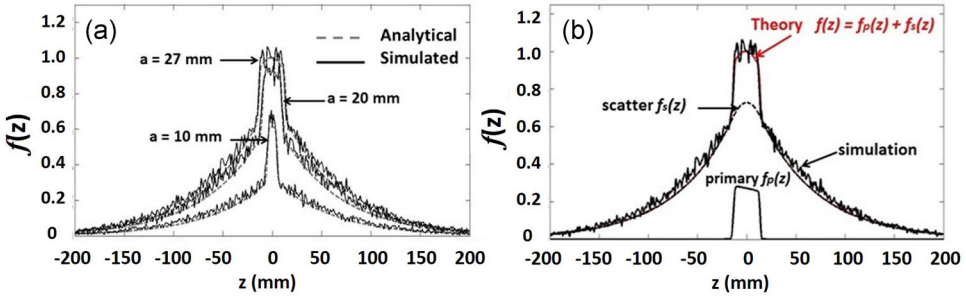

FIGURE 3 (a) Analytical and simulated dose profiles for 10, 20, and 27 mm of collimation projected onto the AOR. (b) Contribution of primary and scatter component on the dose profile for a cylindrical phantom with 32 cm diameter at 120 kV and 27 mm of collimation projected onto the AOR

Discovery CT750 HD, $F = 541$ mm and $F_c = 162$ mm, see Table 2.

3.1.3 | Validation of the bowtie filter position based on $CTDI_{100}$ ratios

As mentioned in Section 2.2.2, a preliminary validation of the x-ray source model was done comparing the ratios $CTDI_{100,c}/CTDI_{100,p}$ and $CTDI_w/CTDI_{100,air}$ ensuing from simulated and measured data from the GE Discovery CT750 HD scanner and also with CTDosimetry[60] data. The average difference of these ratios for body and head protocols between the simulated and measured data varied from 13% to 17% and the comparison of simulated and CTDosimetry data yielded discrepancies that ranged from 10% to 13%.

3.1.4 | Validation based on OSLD Dose Distributions

Figure 4 compares central and peripheral dose distributions in head phantom ($nT = 20$ mm) and body ($nT = 40$ mm) phantoms, respectively, both at 120 kV. Similar comparative curves were obtained for all simulated-measured pairs. They agree better than 19% for both central and peripheral axes.

Figure 5 shows a comparison among primary dose distributions from measurements using OSL ribbons, computed from analytical equations, and computed from MC simulation. Table 4 presents the values of a resulting from the measured, analytical, and simulated primary dose distributions. This parameter is computed as the FWHM of the measured and simulated distributions. The values of a adopted in the equations used to compute the analytical distributions are consistent with the arguments presented in Appendix A of Dixon et al.[21] Table 4 also shows the over-beaming factor, a/nT, where nT is the nominal beam width. These factors are compared to the over-beaming factor for the GE VCT scanner determined by Dixon and Ballard.[68] From Table 4, 5% and 10% of differences between a and nT were identified for $nT = 40$ mm and $nT = 20$ mm, respectively. These values are close to those measured by Dixon and Ballard in a GE VCT scanner that found 5.3% and 12%.

3.1.5 | Validation based on thimble ion chamber measurements

Figure 6 compares simulated and measured results of $H(L)$ for a body protocol with 120 kV, 300 mA, 64 × 0.625 mm as collimation and pitches of 0.516 and 0.984. The dose rate profile was measured with the ion chamber located in the center position and in the periphery of the three-section body phantom for scan lengths of 100, 150, 240, 350, and 450 mm. All results are compatible within 3% considering the combined uncertainty from measured and simulated data.

3.2 | Simulated accumulated dose distributions according to the clinical head and body procedures

Figure 7a and b presents simulated accumulated dose distributions computed along the central and peripheral axes, respectively, of the infinitely long head phantom for 10 rotations of the x-ray source adopting pitch values of 0.531, 0.969, and 1.375 and for 120 kV. The total absorbed dose in the phantom does not depend on the pitch value, but it depends on the number of rotations (fixing the other parameters). This fact can be verified by the numerical integration of the distributions presented in Figures 7a and b. The integration of these distributions result in the same areas, independently of the pitch value. For lower pitch values the absorbed dose is more concentrated about $z = 0$. In contrast, for high pitch values, the absorbed dose is broader. The same statement is visualized in Figures 7c and d, in which for the infinitely long body phantom, beam width $nT = 40$ mm and

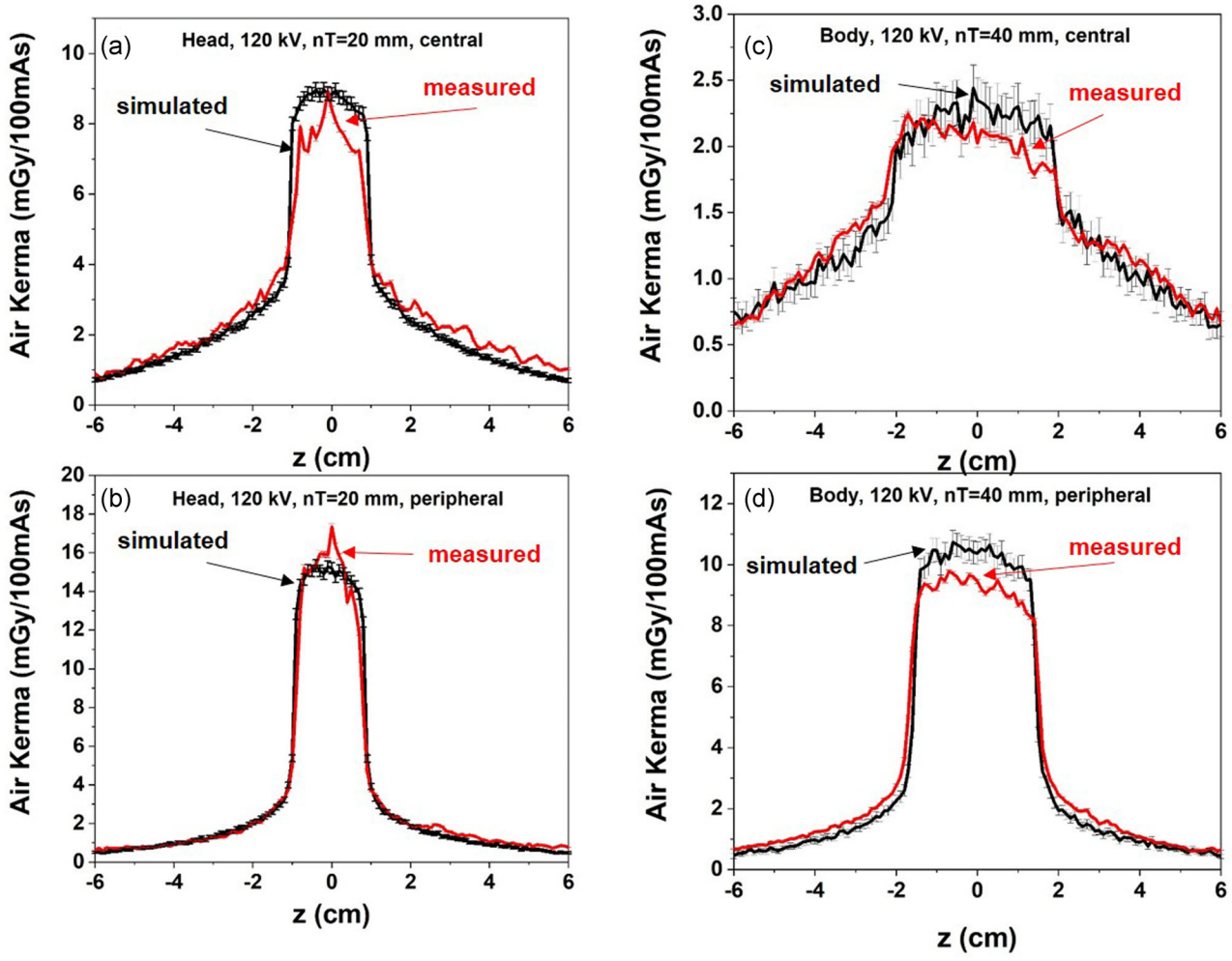

FIGURE 4 Comparison between the simulated and OSL measured dose distributions. (a) Central and (b) Peripheral dose profiles in a head CTDI phantom at 120 kV and $nT = 20$ mm beam width and (c) central and (d) peripheral dose profile in a body CTDI phantom at 120 kV and $nT = 40$ mm beam width

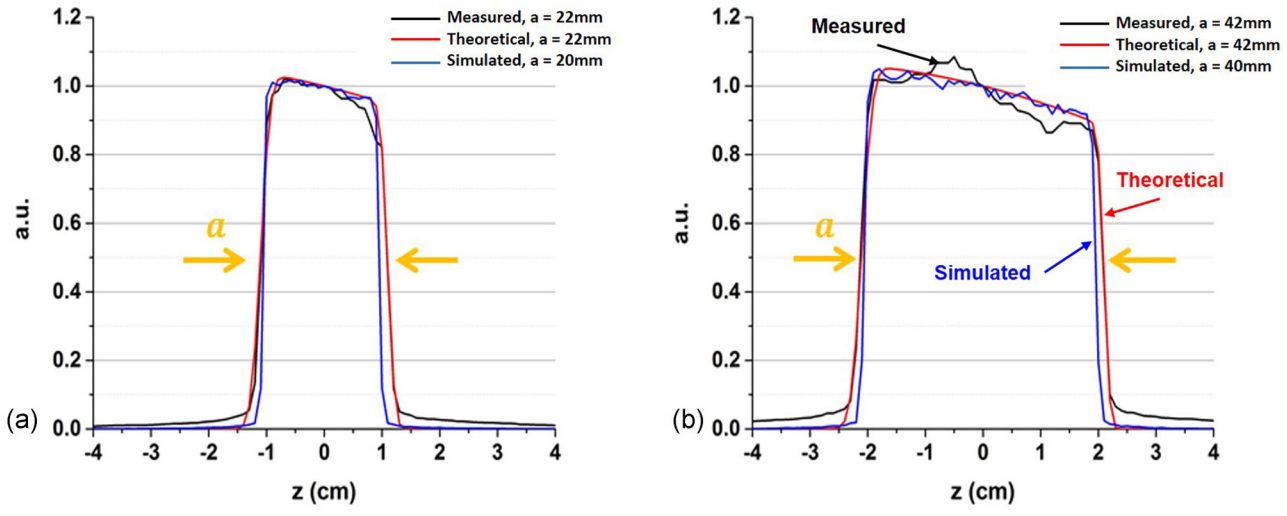

FIGURE 5 Measured, analytical, and simulated primary dose distributions (a) for head bowtie filter at nominal beam width $nT = 20$ mm and (b) body bowtie filter at nominal beam width $nT = 40$ mm. The experimental dose distributions were measured with OSL ribbons

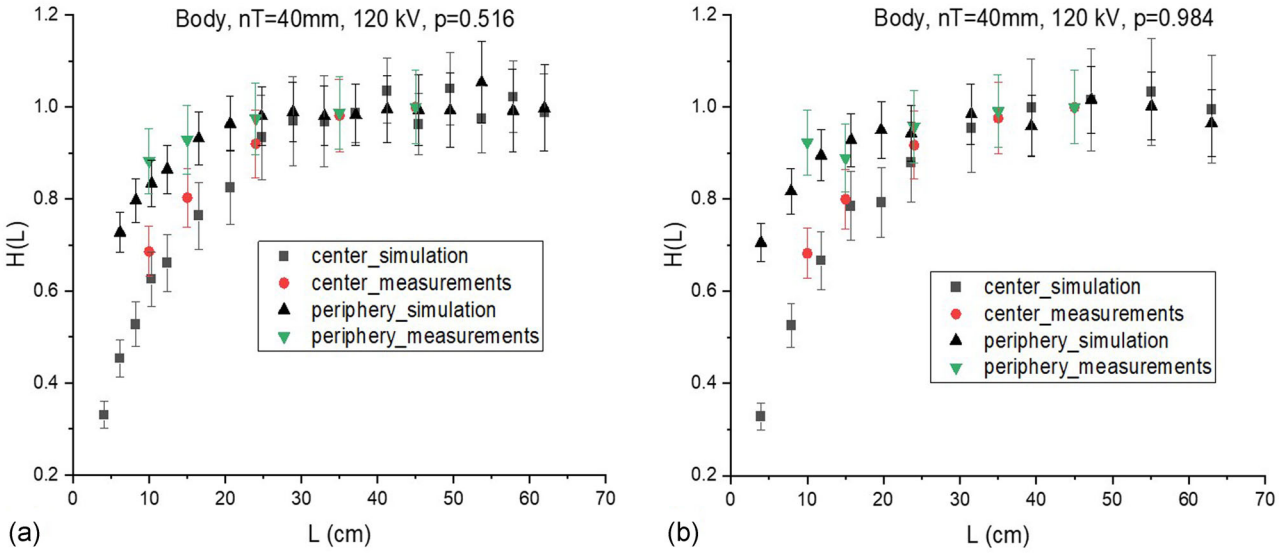

FIGURE 6 Comparative results from simulated and measured $H(L)$ using a body protocol with 120 kV, 300 mA, 64 × 0.625 mm as collimation and pitches of (a) 0.516 and (b) 0.984. The measurements were done using the thimble ion chamber

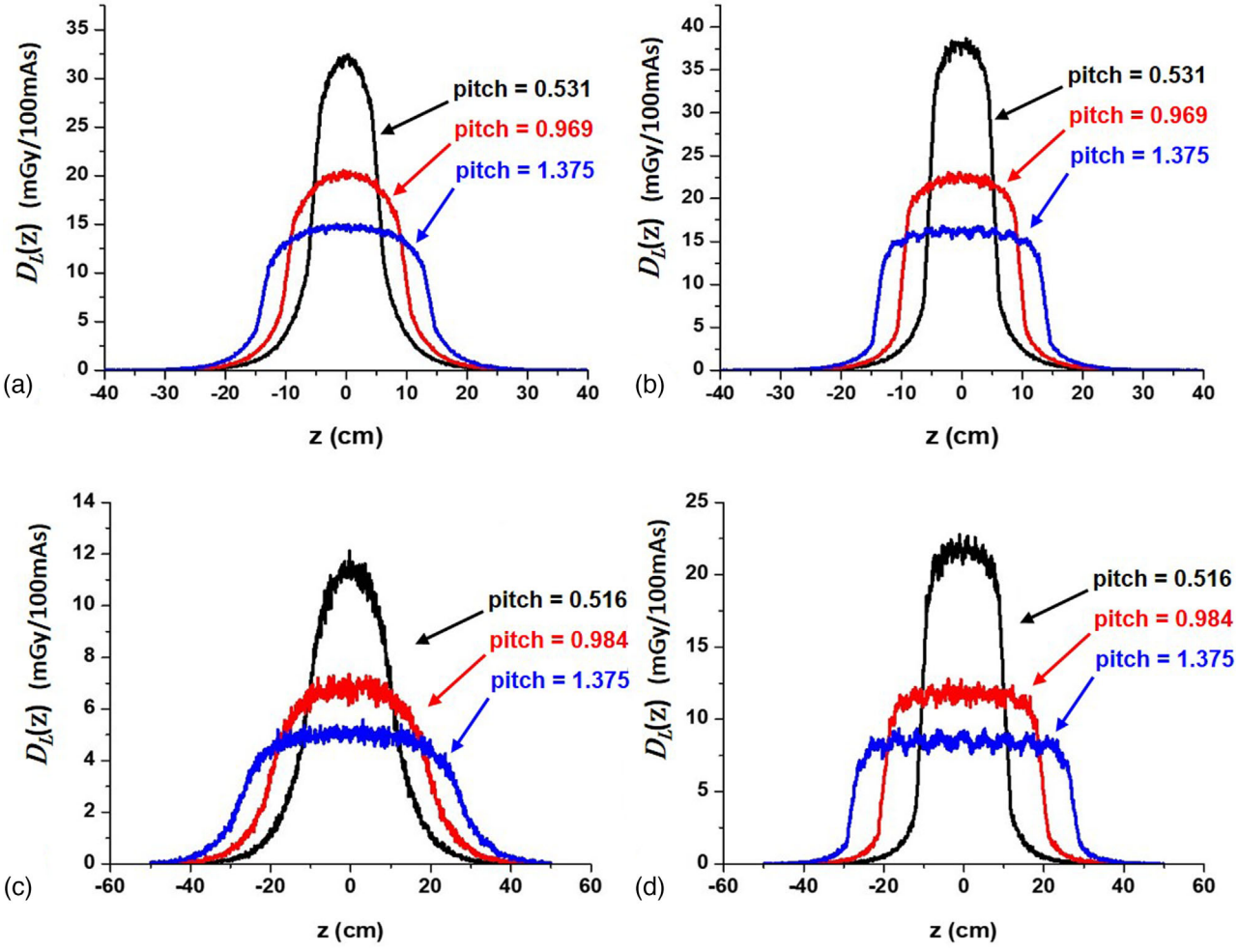

FIGURE 7 MC simulated accumulated dose distributions, $D_L(z)$, in terms of air kerma (mGy/100 mAs) at 120 kV computed along the (a) central axis and (b) peripheral axis for pitch values of 0.531, 0.969, and 1.375 for helical protocol in the head phantom with beam width 20 mm and along the (c) central axis and (d) peripheral axis for pitch values of 0.516, 0.984, and 1.375 for helical protocol in the body phantom with beam width 40 mm. Both helical and axial dose profile correspond to 10 rotations ($n = 10$)

TABLE 4 Collimator aperture, a, projected onto the AOR and over-beaming factor, a/nT, evaluated in the present work for the GE Discovery CT750 HD scanner and compared with Dixon and Ballard[68]

		This work					
		Simulated		Analytical or measured		Dixon and Ballard[68]	
Acquisition Collimation $n \times T$ **(mm)**	nT (mm)	a (mm)	a/nT	a (mm)	a/nT	a (mm)	a/nT
64×0.625	40	40	1	42.0(5)	1.05	42.13	1.05
32×0.625	20	20	1	22.0(5)	1.10	22.39	1.12

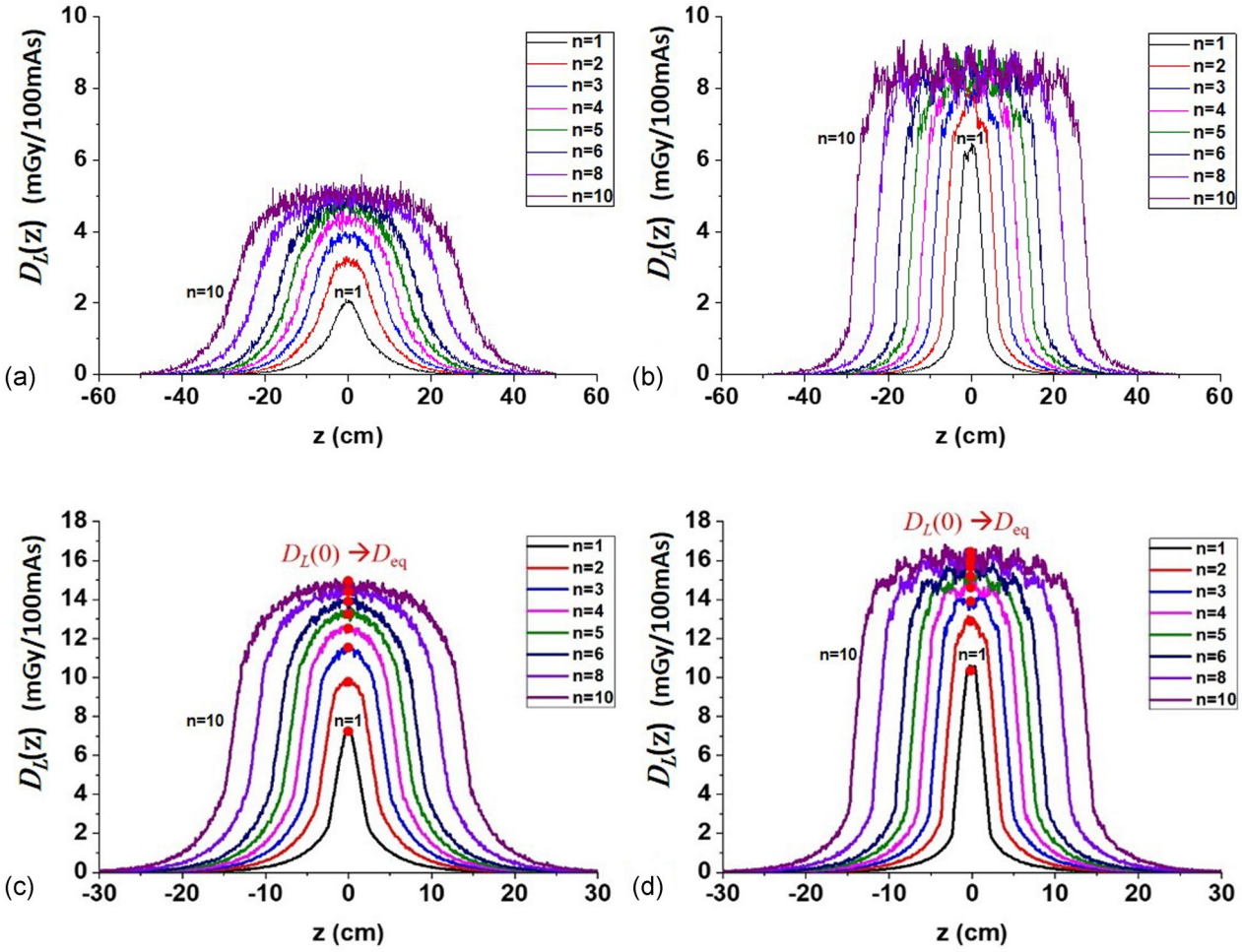

FIGURE 8 Accumulated dose distributions, $D_L(z)$, obtained by MC simulation of CT helical examinations with pitch = 1.375 at 120 kV. The data were obtained for the indicated numbers of x-ray source rotations, n, along the (a) central axis and (b) peripheral axis of the body infinitely long phantom using nT = 40 mm and (c) central axis and (d) peripheral axis of the head infinitely-long phantom using nT = 20 mm

120 kV x-ray spectrum. Note that, for p = 1.375, valleys are identified in the peripheral profile for both head and body protocols. These valleys appear since, in this case, the patient table displacement during one x-ray source rotation is wider than the beam width.

Figure 8 displays a set of 1–10 x-ray source rotations accumulated dose distributions, $D_L(z)$, computed from MC simulation along the central and peripheral axes of the infinitely long body and head phantoms, respectively. The simulations were done for a 1.375 pitch value, 120 kV x-ray spectrum, beam width of 40 mm (body phantom) and 20 mm (head phantom). In each plot, the region of interest of investigation of the profiles were concentrated in regions around the origin, that is, ±30 cm for head phantom (nT = 20 mm) and ±60 cm for body phantom (nT = 40 mm). Figure 8c and d also shows how the dose at z = 0 from the accumulated profile at the central and peripheral axes reach an

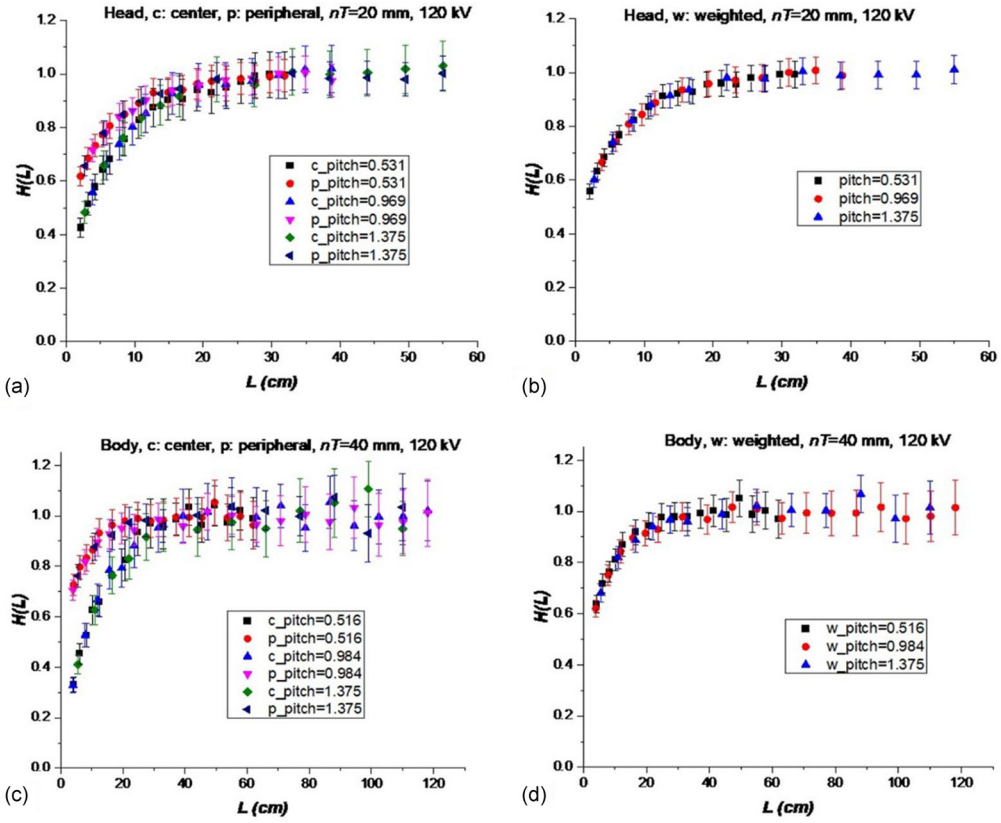

FIGURE 9 Ratio Maximum Dose at $z = 0$ to Equilibrium Dose, $H(L)$, for the 120 kV spectra at (a) central and peripheral positions and (b) weighted by the $CTDI_w$ coefficients for pitch values 0.531, 0.969, and 1.375 for the head phantom and (c) central and peripheral positions and (d) weighted by the $CTDI_w$ coefficients for pitch values 0.516, 0.984, and 1.375 for the body phantom

asymptotic value when the number n of x-ray source rotations increases.

3.3 | AAPM Report 111 and 200 dose metrics calculated from the accumulated dose distributions

The MC simulation of the helical scan mode was performed for pitch values of 0.531, 0.969, and 1.375 for the head protocol, and 0.516, 0.984, and 1.375 for the body protocols using x-ray spectra of 80, 100, 120, and 140 kV. The corresponding $H(L) = D_L(0)/D_{eq}$ ratio of each protocol were calculated. Figure 9 presents $H(L)$ calculated in the central and peripheral axes of the infinitely long head and body CTDI phantom obtained for 120 kV and all studied pitch values.

A practical procedure to compute D_{eq} relies on the linear relation between the dose-line integral, DLI_i, and L. The DLI is defined (see supplemental material #2) as the integral over $-\infty < z < \infty$ of the accumulated dose profile $D_L(z)$ resulting from a helical CT scan acquisition of scan length L. As DLI is proportional to L with term of proportionality being the equilibrium dose, D_{eq}, this value can be obtained from simple linear regression. Therefore, central-D_{eq} ($D_{eq,c}$), peripheral-D_{eq} ($D_{eq,p}$), and weighted-D_{eq} ($D_{eq,w}$) were computed for the infinitely long head and body phantoms using this procedure. The corresponding results are presented in Table 5.

Table 6 lists the equilibrium scanning length (L_{eq}) and the scatter fraction (α) that were obtained by fitting the approach to equilibrium function, $H(L)$. The values for L_{eq} and α were assessed from $H(L)$ that were computed for the central and peripheral axes of the CTDI phantoms.

It is instructive to compute the equilibrium dose-pitch product, $\hat{D}_{eq}$, to have representative values as a function of the tube voltages. These values can be used in CT acceptance tests or comparative clinical protocol to evaluate the associated doses at any pitches values. Table 7 presents the mean values of the $\hat{D}_{eq}$ for head ($nT = 20$ mm) and body ($nT = 40$ mm) helical protocols.

4 | DISCUSSION

The MC dose distributions allowed the calculation of derived functions and dose-related parameters proposed by AAPM Reports 111 and 200. Heel effect, focal

TABLE 5 Results of equilibrium dose (D_{eq}) in units of (mGy/100 mAs) assessed by fitting DLI versus L. The helical acquisition parameters for the head protocol were pitch values of 0.531, 0.969, and 1.375 with beam width of 20 mm, and for the body protocol pitch values were 0.516, 0.984, and 1.375 and beam width of 40 mm. In both cases x-ray spectra of 80, 100, 120, and 140 kV were considered. The coefficient of determination of the fitting was ≈1 for all cases. The values in parenthesis correspond to the estimated uncertainty ($k = 1$)

D_{eq} (mGy/100mAs)								
	Head protocols				Body protocols			
Voltage	Pitch	$D_{eq,c}$	$D_{eq,p}$	$D_{eq,w}$	Pitch	$D_{eq,c}$	$D_{eq,p}$	$D_{eq,w}$
80 kV	0.531	12.8(0.5)	15.7(0.5)	14.8(0.4)	0.516	4.0(0.2)	7.3(0.2)	6.2(0.1)
	0.969	7.0(0.3)	8.6(0.3)	8.1(0.2)	0.984	2.1(0.1)	3.8(0.1)	3.3(0.1)
	1.375	5.0(0.2)	6.1(0.2)	5.7(0.1)	1.375	1.5(0.1)	2.7(0.1)	2.3(0.1)
100 kV	0.531	24.6(1.0)	27.9(0.8)	26.8(0.6)	0.516	9.1(0.4)	14.7(0.4)	12.8(0.3)
	0.969	13.5(0.6)	15.3(0.5)	14.7(0.3)	0.984	4.8(0.2)	7.7(0.2)	6.7(0.2)
	1.375	8.4(0.3)	9.5(0.3)	9.1(0.2)	1.375	3.4(0.1)	5.5(0.1)	4.8(0.1)
120 kV	0.531	38.8(1.6)	42.4(1.2)	41.2(1.0)	0.516	13.4(0.5)	22.7(0.7)	19.6(0.5)
	0.969	21.3(0.9)	23.3(0.7)	22.6(0.5)	0.984	7.0(0.3)	11.9(0.3)	10.3(0.2)
	1.375	15.0(0.6)	16.4(0.5)	15.9(0.4)	1.375	5.0(0.2)	8.5(0.2)	7.4(0.2)
140 kV	0.531	55.3(2.3)	59.1(1.7)	57.8(1.4)	0.516	24.2(1.0)	32.5(0.9)	29.7(0.7)
	0.969	30.3(1.2)	32.3(1.0)	31.6(0.8)	0.984	12.7(0.5)	17.0(0.5)	15.6(0.4)
	1.375	21.3(0.9)	22.8(0.7)	22.3(0.5)	1.375	9.1(0.4)	12.2(0.3)	11.1(0.3)

TABLE 6 Results of equilibrium scan length, L_{eq}, and scatter fraction, α, for head and body helical acquisition parameters. The values in parenthesis correspond to the estimated uncertainty ($k = 1$)

		Head protocols					Body protocols			
		Center		Peripheral			Center		Peripheral	
Voltage	Pitch	L_{eq} (cm)	α	L_{eq} (cm)	α	Pitch	L_{eq} (cm)	α	L_{eq} (cm)	α
80 kV	0.531	28.1(0.7)	0.76(1)	24.1(0.8)	0.53(1)	0.516	44.0(2.3)	0.94(3)	26.1(1.9)	0.49(3)
	0.969	27.2(1.2)	0.75(3)	27.4(2.3)	0.48(4)	0.984	41.7(2.1)	0.96(3)	29.5(3.4)	0.47(4)
	1.375	27.5(0.7)	0.76(1)	26.8(1.4)	0.50(2)	1.375	46.1(2.9)	0.95(4)	39.4(6.4)	0.39(5)
100 kV	0.531	27.7(0.8)	0.77(1)	25.7(1.3)	0.52(2)	0.516	41.0(1.1)	1.00(3)	26.7(1.7)	0.51(3)
	0.969	27.6(1.0)	0.77(2)	29.5(1.6)	0.47(2)	0.984	42.7(1.5)	0.97(2)	32.0(2.8)	0.48(3)
	1.375	27.5(0.7)	0.76(1)	26.8(1.4)	0.50(2)	1.375	42.8(2.8)	0.98(4)	36.0(3.0)	0.40(3)
120 kV	0.531	29.7(0.7)	0.76(1)	27.7(1.0)	0.50(1)	0.516	43.9(2.2)	0.98(3)	28.9(2.3)	0.49(3)
	0.969	28.1(1.0)	0.77(2)	30.1(1.4)	0.47(2)	0.984	45.0(2.1)	0.95(2)	35.0(2.9)	0.46(3)
	1.375	28.5(1.0)	0.76(2)	27.6(1.1)	0.51(1)	1.375	48.9(3.8)	0.92(5)	35.8(6.1)	0.44(7)
140 kV	0.531	28.7(0.8)	0.75(1)	28.0(1.0)	0.50(1)	0.516	45.8(2.3)	0.97(3)	29.8(2.2)	0.49(3)
	0.969	30.5(1.2)	0.71(2)	28.8(2.0)	0.48(3)	0.984	47.2(1.9)	0.95(2)	38.7(2.8)	0.44(2)
	1.375	28.9(0.6)	0.75(1)	27.3(1.3)	0.50(2)	1.375	46.3(3.3)	0.95(4)	37.2(2.8)	0.42(3)

TABLE 7 Average equilibrium dose-pitch product, $\hat{D}_{eq}$, as a function of typical pitch values for head ($nT = 20$ mm) and body ($nT = 40$ mm) helical protocols. The values in parenthesis correspond to the estimated uncertainty ($k = 1$)

	Head ($nT = 20$ mm)			Body ($nT = 40$ mm)		
Voltage (kV)	$\hat{D}_{eq,c}$ (mGy/100 mAs)	$\hat{D}_{eq,p}$ (mGy/100 mAs)	$\hat{D}_{eq,w}$ (mGy/100 mAs)	$\hat{D}_{eq,c}$ (mGy/100 mAs)	$\hat{D}_{eq,p}$ (mGy/100 mAs)	$\hat{D}_{eq,w}$ (mGy/100 mAs)
80	6.8(0.5)	8.3(0.4)	7.8(0.3)	2.1(0.1)	3.8(0.2)	3.2(0.1)
100	12.6(0.9)	14.2(0.7)	13.7(0.6)	4.7(0.3)	7.6(0.3)	6.6(0.3)
120	20.6(1.5)	22.5(1.2)	21.9(0.9)	6.9(0.5)	11.7(0.5)	10.1(0.4)
140	29.3(2.1)	31.3(1.6)	30.7(1.3)	12.5(0.9)	16.8(0.8)	15.3(0.6)

spot size and angle, and x-ray spectrum are factors that affect the shape of the primary dose profile produced by a single axial rotation. The same factors were considered for the MC model validation that was done by direct comparison of simulated and analytical distributions. This validation demonstrate that these distributions were compatible within 1%. In addition, comparisons among primary dose distributions from OSL measurements, analytical equations, and MC simulations were done for the evaluation of the over-beaming factor (Figure 5 and Table 4). These comparisons resulted in 5% and 10% differences between a and nT for $nT = 40$ mm and $nT = 20$ mm, respectively. These dose distributions were used to calculate the metrics proposed in the AAPM Reports 111 and 200.

Equilibrium dose (D_{eq}), equilibrium dose-pitch product (pD_{eq}), the equilibrium scanning length (L_{eq}), and the scatter fraction (α) were determined from the simulated distributions (Tables 5–7). A comprehensive study of these new dosimetric indices was performed for the head and body helical protocols with $nT = 20$ mm and $nT = 40$ mm that are the common values in the clinical practice. In general terms, the clinical parameters such as pitch, beam intensity, and kV affect the D_{eq} values. The increase of the pitch decreases the D_{eq} value while the beam intensity and kV increase its value. The approach to equilibrium function, $H(L)$, does not depend on the pitch values, but depends on the phantom position, central or peripheral. L_{eq} and α were determined by fitting the $H(L)$ curve with an exponential model.

From the obtained results, the dependencies with the pitch value for both α and L_{eq} (Table 6) appear to be more relevant for the peripheral profile in the body phantom. Note that the parameter α is higher for the central axis than for the peripheral axes for both head and body phantoms. This makes sense because the contribution of the scatter radiation to the deposited dose at the central region is higher than at the periphery. The scatter fraction, α, at the central axis for the body phantom case is higher than for the head phantom case. Again, this is expected because the x-ray beam presents more scatter into the body phantom than in the head case. The parameter α is quite insensitive to the tube voltage, for the head and body protocols, as shown by Li et al.[69] However, our α results have a small dependence with the pitch value, that was not evaluated by other authors. The center and peripheral L_{eq} has small dependence with the x-ray spectra and pitch values for the head and body helical protocol.

The scatter-to-primary ratio, η, can be derived from its relationship with the scatter fraction, since $\alpha = \eta/(1+\eta)$. Considering the head protocols for a given spectrum, the values of η appear to have a small sensitivity to the pitches (0.516, 0.969, and 1.375), with maximum variations around 5%. An exception was found in the 140 kV spectra, with a maximum variation of η of 18%. Considering the peripheral axis, this parameter presented maximum variations between 8% and 18% considering different spectra and pitches. This behavior does not happen in the body protocols, with maximum variations in the range of 35–76% in the central axis and 11–35% in the peripheral axis. The η at central axis is approximately three times higher than at the peripheral axis for the head protocols with low dependency with the x-ray spectra and pitches. For the body protocols, these differences are much more pronounced, reaching to be more than 20 times higher in the central axis than in the periphery and presenting dependence with pitches and x-ray spectra. It means that at the central axis the radiation scattered by the body phantom material has more contribution to the dose than the produced by the primary beam.

Table 8 compares values of η derived from scatter fractions and compare them to similar data found in the literature. The table also compares the present L_{eq} results with data from the literature. In the case of η for the head CTDI phantom, good agreement is reached with data from Li et al.[69] and Tsai et al.[70] for the central and peripheral axes. The data from the literature were computed or measured for a pitch value equal 1. Comparison of the L_{eq} in the case of body CTDI phantom at the central axis shows good agreement with data from MC simulation[69,71] and experimental measurements.[68] In the case of peripheral axis, L_{eq} this work differs in approximately 5 cm with respect to data from the literature. It is important to mention that the data from Li et al.[69] were derived from direct integration of the single dose profile using a 1-mm beam width and pitch equal to 1. Nevertheless, the authors show that the variation of L_{eq} with the beam width (from 1 to 40 mm) is less than 1 cm at 120 kV, which is covered by the uncertainty from their results. Data from Dixon and Ballard[68] were acquired at 120 kV, 400 mAs, large FOV, large focal spot, $nT = 64 \times 0.625$ mm $= 40$ mm ($p = 0.984$ on center and $p = 0.516$ on periphery), $nT = 32 \times 0.625$ mm $= 20$ mm ($p = 0.969$ on center and $p = 0.531$ on periphery). Table 8 also shows good agreement for L_{eq} between the present work and data computed by Li et al.[69] for the head CTDI phantom at the central axis. In general, the shape of the central accumulated profile is influenced by the scatter radiation. The contribution of this scatter radiation is around 3.3 times the contribution of the primary radiation for the head phantom.

5 | CONCLUSIONS

In this study, dose distributions in infinitely long cylindrical PMMA dosimetry phantoms resulting from single axial and helical CT acquisition of a MDCT were obtained by MC simulations. The proposed model and its multiple-validation strategies demonstrate to be a robust contribution to the CT dosimetry using new proposed

TABLE 8 Scatter to primary ratio, η, and equilibrium scanning length, L_{eq}, for head and body helical protocols

	Phantom	Location	This work	(Li, et al., 2013)[69]	(Dixon and Ballard, 2007)[68]	(Dixon and Boone, 2010)[72]
η	**Head**	Periphery	0.9–1.13	1.21	0.9–1.3	…
		Center	3.0–3.3	3.78	3.0	…
	Body	Periphery	0.6–1.1	1.23	0.8–1.1	1.5
		Center	11—19	8.21	5.7	13.0
L_{eq} **(cm)**	**Head**	Periphery	30.1(1.4)	24.1(1.0)	—	—
		Center	28.1(1.0)	28.5(1.0)	—	—
	Body	Periphery	35.0(2.9)	28.4(1.0)	28.0	30.0
		Center	45.0(2.1)	42.0(1.0)	44.8	47.0

methods. It also demonstrates the possibility to obtain estimates of the rise to equilibrium functions and derived metrics using complementary procedures to the use of a 60-cm long phantom.

Previous studies[8,20] put in evidence the limitations of the $CTDI_{100}$ method to determine the dose delivered by a CT scanner. Therefore, quantities derived from the $CTDI_{100}$ propagate that limitation. In this study, it was demonstrated that the efficiency of the $CTDI_{100}$ measurement in MDCT scanners is 80.6% and 87.8% at central and peripheral axes, respectively, for head phantom with $nT = 20$ mm, 56.5% and 86.2% at central and peripheral axes, respectively, for body phantom with $nT = 40$ mm, all data for 120 kV x-ray spectrum. This limitation reinforces the advantages of the metrics proposed on the AAPM Reports 111[9] and 200.[10]

It is instructive to compute the equilibrium dose-pitch product, $\hat{D}_{eq}$, to have representative values of this quantity as a function of the tube voltages and independency of the pitch and collimation. These values can be used in CT quality control and acceptance tests or in comparative analysis of clinical protocols. Table 7 presents values of the $\hat{D}_{eq}$ for head and body helical protocols.[9] Given its proportionality to the dose delivered in a CT procedure independently of the pitch, this metric could be useful for future association with SSDE and organ doses.

Tian et al.[72] also proposed a new approach to assess patient-specific CT organ doses in prospective and retrospective ways based on the computation of the accumulated dose profile. The purpose is to convolve the single axial dose profile with a rectangular function to produce the accumulated dose distributions that serves as a good estimators of dose characteristics along the scanning length.

The multiple-validation strategy adopted here demonstrate to be an important contribution to CT dosimetry using the new CT dose metrics proposed in the AAPM Reports 111 and 200. Additionally, the application of the AAPM Reports 111 and 200 methodology using traditional PMMA phantoms to access the approach to equilibrium function and its derived data associated to clinical procedures is an additional improvement to the popularization of these new quantities. This approach can be incorporated by medical physicists in quality control or quality assurance programs during the migration process of the current CTDI-based methodology to the new proposed metrics using the ICRU/AAPM phantom. Finally, the methods developed in the present work using MC simulations may contribute in future investigations to improve organ dose estimation from different protocols and CT models. This framework can be associated to SSDE data and image quality evaluations from these procedures as an advanced method to CT dose/image quality optimization initiatives.

In conclusion, the developed MC model shows excellent compatibility with both measurements and literature quantities defined by AAPM Reports 111 and 200. These results confirm the robustness and versatility of the proposed modeling method and emphasize the importance of a detailed and careful validation of any MC modeling in order to reproduce accurate information.

ACKNOWLEDGEMENTS

The authors would like to acknowledge the grants 2010/12237-7 and 2018/05982-0 from The São Paulo Research Foundation (FAPESP) and the National Commission of Nuclear Energy (CNEN) for the scholarship 1341001551/2015. They also thank CNPQ for research grant 315096/2018-7, and CNPQ/FAPESP funding of the project by INCT - Metrology of Ionizing Radiation in Medicine (grant number 2008/57863-2). JMF-V was supported by the Spanish Ministerio de Ciencia, Innovación y Universidades, grant no. PGC2018-096788-B-I00. The authors also thank the Institute of Radiology of the School of Medicine of the University of São Paulo for allowing the validation measurements. We are grateful to Prof. Ricardo A. Terini for providing the experimental x-ray spectra and to Prof. Alessandra Tomal for her scientific support regarding the use of PENELOPE and for her kind review of the manuscript.

CONFLICT OF INTEREST

The authors have no conflicts to disclose

DATA AVAILABILITY STATEMENT

Research data are not shared

REFERENCES

1. Computed tomography (CT) exams. 2018. Accessed December 02, 2020 https://www.oecd-ilibrary.org/content/data/3c994537-en.
2. NCRP. Medical Radiation Exposurers of Patients in the United States. National Council on Radiation Protection and Measurements; 2019.
3. Rehani MM, Szczykutowicz TP, Zaidi H. CT is still not a low-dose imaging modality. *Med Phys*. 2020; 47(2): 293-296.
4. Brambilla M, Vassileva J, Kuchcinska A, Rehani MM. Multinational data on cumulative radiation exposure of patients from recurrent radiological procedures: call for action. *Eur Radiol*. 2020; 30(5): 2493-2501.
5. Järvinen H, Vassileva J, Samei E, Wallace A, Vano E, Rehani M. Patient dose monitoring and the use of diagnostic reference levels for the optimization of protection in medical imaging: current status and challenges worldwide. *J Med Imag*. 2017; 4(3): 031214.
6. Dixon RL. *The Physics of CT Dosimetry: CTDI and Beyond*. 1st ed. Boca Raton, FL: CRC Press; 2019.
7. Leitz W, Axelsson B, Szendro G. Computed tomography dose assessment - a practical approach. *Radiat Prot Dosim*. 1995; 57(1-4): 377-380.
8. Dixon RL. A new look at CT dose measurement: beyond CTDI. *Med Phys*. 2003; 30(6): 1272-1280.
9. AAPM. Comprehensive methodology for the evaluation of radiation dose in X-ray computed tomography. *AAPM Task Group 111 (AAPM Report 111)*. American Association of Physicists in Medicine; 2010.
10. AAPM. The design and use of the ICRU/AAPM CT radiation dosimetry phantom: an implementation of AAPM report 111. In: Bakalyar DM, Angel E, Boedeker KL, eds. *The Report of AAPM Task Group 200*. AAPM; 2020.
11. Costa PR. Computer tomography phantom applications. In: DeWerd LA, Kissick M, eds. *The Phantoms of Medical and Health Physics: Devices for Research and Development*. New York, NY: Springer New York; 2014:123-142.
12. Tomal A, Costa PR. Phantoms for image quality and dose assessment. In: Russo P, ed. *Handbook of X-ray Imaging: Physics and Technology*. Boca Raton FL: CRC Press; 2017:1135-1157.
13. McCollough CH, Leng S, Yu L, Cody DD, Boone JM, McNitt-Gray MF. CT dose index and patient dose: they are not the same thing. *Radiology*. 2011; 259(2): 311-316.
14. Smith-Bindman R, Miglioretti DL. CTDIvol, DLP, and Effective Dose Are Excellent Measures for Use in CT Quality Improvement. *Radiology*. 2011; 261(3): 999-999. https://doi.org/10.1148/radiol.11111055
15. AAPM. Size-specific dose estimates (SSDE) in pediatric and adult body CT examinations. AAPM Task Group 204 (AAPM Report 204); 2011.
16. McCollough C, Bakalyar DM, Bostani M, et al. Use of water equivalent diameter for calculating patient size and size-specific dose estimates (SSDE) in CT: The report of AAPM task group 220. *AAPM Rep*. 2014: 6-23.
17. Andersson J, Pavlicek W, Al-Senan R, et al. Estimating Patient Organ Dose with Computed Tomography: A Review of Present Methodology and Required DICOM Information. One Physics Ellipse, College Park, MD: AAPM-EFOMP, 2019
18. Boone JM, Strauss KJ, Hernandez AM, et al. *Dose Estimate (SSDE) for Head CT*. The Report of AAPM Task Group 293 American Association of Physicists in Medicine; 2019.
19. Boone JM. The trouble with CTDI100. *Med Phys*. 2007; 34(4): 1364-1371.
20. Dixon RL. Restructuring CT dosimetry—A realistic strategy for the future requiem for the pencil chamber. *Med Phys*. 2006; 33(10): 3973-3976.
21. Dixon RL, Munley MT, Bayram E. An improved analytical model for CT dose simulation with a new look at the theory of CT dose. *Med Phys*. 2005; 32(12): 3712-3728.
22. Dixon RL, Boone JM. Cone beam CT dosimetry: a unified and self-consistent approach including all scan modalities—with or without phantom motion. *Med Phys*. 2010; 37: 2703-2718.
23. IAEA. Implementation of the International Code of Practice on Dosimetry in Diagnostic Radiology (TRS 457): review of test results. Report n.4; 2011..
24. AAPM. The measurement, reporting, and management of radiation dose in CT. AAPM Task Group 23 (AAPM Report 96); 2008.
25. Dixon RL, Boone JM, Kraft RA. Dose equations for shift-variant CT acquisition modes using variable pitch, tube current, and aperture, and the meaning of their associated CTDIvol. *Med Phys*. 2014; 41(11).
26. Boone JM, Brink JA, Edyvean S, et al. *Radiation Dose And Image-Quality Assessment In Computed Tomography*. International Commission On Radiation Units And Measurements; 2012.
27. Sechopoulos I, Ali ES, Badal A, et al. Monte Carlo reference data sets for imaging research: executive summary of the report of AAPM Research Committee Task Group 195. *Med Phys*. 2015; 42(10): 5679-5691.
28. Sechopoulos I, Rogers DWO, Bazalova-Carter M, et al. RECORDS: improved reporting of MontE CarlO RaDiation transport studies: report of the AAPM Research Committee Task Group 268. *Med Phys*. 2018; 45(1): e1-e5.
29. Gonzales AHL. *Simulation and Validation of Dose Profiles and their Use to Estimate Dosimetric Quantities for Computed Tomography*. Instituto de Física, Universidade de São Paulo; 2019.
30. Samei E, Bakalyar D, Boedeker KL, et al. Performance evaluation of computed tomography systems: summary of AAPM Task Group 233. *Med Phys*. 2019; 46(11): e735-e756.
31. Ria F, Solomon JB, Wilson JM, Samei E. Technical Note: validation of TG 233 phantom methodology to characterize noise and dose in patient CT data. *Med Phys*. 2020; 47(4): 1633-1639.
32. DeMarco JJ, Cagnon CH, Cody DD, et al. A Monte Carlo based method to estimate radiation dose from multidetector CT (MDCT): cylindrical and anthropomorphic phantoms. *Phys Med Biol*. 2005; 50(17): 3989-4004.
33. Abadi E, Harrawood B, Sharma S, Kapadia A, Segars WP, Samei E. DukeSim: a realistic, rapid, and scanner-specific simulation framework in computed tomography. *IEEE Trans Med Imaging*. 2019; 38(6): 1457-1465.
34. Salvat F, Sempau J, Fernández-Varea JM. *PENELOPE-2014: A Code System for Monte Carlo Simulation of Electron and Photon Transport*. Workshop, Barcelona; 2015.
35. Sempau J, Badal A, Brualla L. A PENELOPE-based system for the automated Monte Carlo simulation of clinacs and voxelized geometries—application to far-from-axis fields. *Med Phys*. 2011; 38(11): 5887-5895.
36. Brualla L, Rodriguez M, Sempau J, Andreo P. PENELOPE/PRIMO-calculated photon and electron spectra from clinical accelerators. *Radiat Oncol*. 2019; 14(1): 6.
37. Brualla L, Salvat F, Palanco-Zamora R. Efficient Monte Carlo simulation of multileaf collimators using geometry-related variance-reduction techniques. *Phys Med Biol*. 2009; 54(13): 4131-4149.
38. Bush K, Zavgorodni SF, Beckham WA. Azimuthal particle redistribution for the reduction of latent phase-space variance in Monte Carlo simulations. *Phys Med Biol*. 2007; 52(14): 4345-4360.
39. Cho SH, Vassiliev ON, Lee S, Liu HH, Ibbott GS, Mohan R. Reference photon dosimetry data and reference phase space data for the 6 MV photon beam from varian clinac 2100 series linear accelerators. *Med Phys*. 2005; 32(1): 137-148.

40. Downes P, Jarvis R, Radu E, Kawrakow I, Spezi E. Monte Carlo simulation and patient dosimetry for a kilovoltage cone-beam CT unit. *Med Phys*. 2009; 36(9Part1): 4156-4167.
41. Kim S, Yoshizumi TT, Yin FF, Chetty IJ. Spiral computed tomography phase-space source model in the BEAMnrc/EGSnrc Monte Carlo system: implementation and validation. *Phys Med Biol*. 2013; 58(8): 2609-2624.
42. Walters BRB, Ding GX, Kramer R, Kawrakow I. Skeletal dosimetry in cone beam computed tomography. *Med Phys*. 2009; 36(7): 2915-2922.
43. Sempau J, Sánchez-Reyes A, Salvat F, ben Tahar HO, Jiang SB, Fernández-Varea JM. Monte Carlo simulation of electron beams from an accelerator head using PENELOPE. *Phys Med Biol*. 2001; 46(4): 1163-1186.
44. Lewis M, Keat N, Edyvean S, *Six to ten slice CT scanner comparison*. IMPACTSCAN; 2006.
45. Atherton JV, Huda W. CT doses in cylindrical phantoms. *Phys Med Biol*. 1995; 40(5): 891-911.
46. Boone JM. Dose spread functions in computed tomography: a Monte Carlo study. *Med Phys*. 2009; 36(10): 4547-4554.
47. Kramer R, Cassola VF, Andrade ME, de Araújo MW, Brenner DJ, Khoury HJ. Mathematical modelling of scanner-specific bowtie filters for Monte Carlo CT dosimetry. *Phys Med Biol*. 2017; 62(3): 781-809.
48. Almansa J, Salvat-Pujol F, Díaz-Londoño G, Carnicer A, Lallena AM, Salvat F. PENGEOM—A general-purpose geometry package for Monte Carlo simulation of radiation transport in material systems defined by quadric surfaces. *Comput Phys Commun*. 2016; 199: 102-113.
49. Tucker DM, Barnes GT, Chakraborty DP. Semiempirical model for generating tungsten target x-ray spectra. *Med Phys*. 1991; 18(2): 211-218.
50. Costa PR, Nersissian DY, Salvador FC, Rio PB, Caldas LVE. Generation of calibrated tungsten target x-ray spectra: modified TBC model. *Health Phys*. 2007; 92: 24-32.
51. Lopez Gonzales AH, Tomal A, Costa PR. Evaluation of characteristic-to-total spectrum ratio: comparison between experimental and a semi-empirical model. *Appl Radiat Isot*. 2015; 100: 27-31.
52. Whiting BR, Evans JD, Dohatcu AC, Williamson JF, Politte DG. Measurement of bow tie profiles in CT scanners using a real-time dosimeter. *Med Phys*. 2014; 41(10): 101915.
53. Whiting BR, Dohatcu AC, Evans JD, Politte DG, Williamson JF. Technical Note: measurement of bow tie profiles in CT scanners using radiochromic film. *Med Phys*. 2015; 42(6Part1): 2908-2914.
54. Yang K, Li X, George XX, Liu B. Direct and fast measurement of CT beam filter profiles with simultaneous geometrical calibration. *Med Phys*. 2017; 44(1): 57-70.
55. Lück F, Kolditz D, Hupfer M, Steiding C, Kalender WA. Experimental validation of a single shaped filter approach for CT using variable source-to-filter distance for examination of arbitrary object diameters. *Phys Med Biol*. 2014; 59(19): 5691-5706.
56. Puerto LR. *Monte Carlo Simulation of the Image Acquisition process of a Dual Energy Computed Tomography Device*. Institute of Physics, University of São Paulo; 2018.
57. Terini RA, Nerssissian DY, Campelo MCS, Morice V, Yoshimura EM. Compton spectrometry applied to clinical CT axial beams from tubes stopped and in revolution. *Radiat Phys Chem*. 2020; 171: 108734.
58. Hernandez AM, Boone JM. Tungsten anode spectral model using interpolating cubic splines: unfiltered x-ray spectra from 20 kV to 640 kV. *Med Phys*. 2014; 41(4): 042101.
59. Omar A, Andreo P, Poludniowski G. A model for the energy and angular distribution of x rays emitted from an x-ray tube. Part II. Validation of x-ray spectra from 20 to 300 kV. *Med Phys*. 2020; 47(9): 4005-4019.
60. Lewis M. CT Dosimetry: ImPACT spreadsheet for calculating organ & effective doses from CT exams, 2017. Accessed February 22, 2019. http://www.impactscan.org/slides/ctdosimetrydenmark/
61. IAEA. Dosimetry in diagnostic radiology: an International Code of Practice, Technical Reports Series No. 457. International Atomic Energy Agency; 2007.
62. Ruan C, Yukihara EG, Clouse WJ, Gasparian PBR, Ahmad S. Determination of multislice computed tomography dose index (CTDI) using optically stimulated luminescence technology. *Med Phys*. 2010; 37(7Part1): 3560-3568.
63. Vrieze TJ, Sturchio GM, McCollough CH. Technical Note: precision and accuracy of a commercially available CT optically stimulated luminescent dosimetry system for the measurement of CT dose index. *Med Phys*. 2012; 39(11): 6580-6584.
64. Kry SF, Alvarez P, Cygler JE, et al. AAPM TG 191: clinical use of luminescent dosimeters: tLDs and OSLDs. *Med Phys*. 2020; 47(2): e19-e51.
65. Yukihara EG, McKeever SWS. Optically stimulated luminescence (OSL) dosimetry in medicine. *Phys Med Biol*. 2008; 53(20): R351-379.
66. Giansante L, Santos JC, Umisedo NK, Terini RA, Costa PR. Characterization of OSL dosimeters for use in dose assessment in computed tomography procedures. *Physica Med*. 2018; 47: 16-22.
67. Bakalyar DM, Solver sample for Deq. Personal Communication. Personal communication ed2020.
68. Dixon RL, Ballard AC. Experimental validation of a versatile system of CT dosimetry using a conventional ion chamber: beyond CTDI100. *Med Phys*. 2007; 34(8): 3399-3413.
69. Li X, Zhang D, Liu B. Monte Carlo assessment of CT dose equilibration in PMMA and water cylinders with diameters from 6 to 55 cm. *Med Phys*. 2013; 40(3): 031903.
70. Tsai HY, Tung CJ, Huang MH, Wan YL. Analyses and applications of single scan dose profiles in computed tomography. *Med Phys*. 2003; 30(8): 1982-1989.
71. Dixon RL, Boone JM. Dose equations for tube current modulation in CT scanning and the interpretation of the associated CTDIvol. *Med Phys*. 2013; 40(11).
72. Tian X, Segars WP, Dixon RL, Samei E. Convolution-based estimation of organ dose in tube current modulated CT. *Phys Med Biol*. 2016; 61(10): 3935-3954.

SUPPORTING INFORMATION

Additional supporting information may be found in the online version of the article at the publisher's website.

How to cite this article: Costa PR, Nersissian DY, Umisedo NK, Gonzales AHL, Fernández-Varea JM. A comprehensive Monte Carlo study of CT dose metrics proposed by the AAPM Reports 111 and 200. *Med Phys.* 2022;49:201–218. https://doi.org/10.1002/mp.15306